PHYSICAL REVIEW B **112**, 035409 (2025)

Editors' Suggestion

Phonon-limited valley lifetimes in single-particle bilayer graphene quantum dots

L. Banszerus,[1,2,*,†] K. Hecker,[1,2,*] L. Wang,[3] S. Möller,[1,2] K. Watanabe,[4] T. Taniguchi,[5]
G. Burkard,[3] C. Volk,[1,2] and C. Stampfer[1,2]
[1]*JARA-FIT and 2nd Institute of Physics, RWTH Aachen University, 52074 Aachen, Germany, EU*
[2]*Peter Grünberg Institute (PGI-9), Forschungszentrum Jülich, 52425 Jülich, Germany, EU*
[3]*Department of Physics, University of Konstanz, 78457 Konstanz, Germany, EU*
[4]*Research Center for Electronic and Optical Materials, National Institute for Materials Science, 1-1 Namiki, Tsukuba 305-0044, Japan*
[5]*Research Center for Materials Nanoarchitectonics, National Institute for Materials Science, 1-1 Namiki, Tsukuba 305-0044, Japan*

(Received 1 May 2024; accepted 5 June 2025; published 10 July 2025)

The valley degree of freedom in two-dimensional (2D) semiconductors, such as gapped bilayer graphene (BLG) and transition metal dichalcogenides, is a promising carrier of quantum information in the emerging field of valleytronics. While valley dynamics have been extensively studied for moderate band gap 2D semiconductors using optical spectroscopy techniques, very little is known about valley lifetimes in narrow band gap BLG, which is difficult to study using optical techniques. Here, we report single-particle valley relaxation times T_1 exceeding several microseconds in electrostatically defined BLG quantum dots using a pulse-gating technique. The observed dependence of T_1 on perpendicular magnetic field can be understood qualitatively and quantitatively by a model in which T_1 is limited by electron-phonon coupling. We identify the coupling to acoustic phonons via the bond length change and via the deformation potential as the limiting mechanisms.

DOI: 10.1103/dkgn-pfjb

I. INTRODUCTION

Charge carriers in two-dimensional (2D) materials with a hexagonal crystal lattice have, in addition to the spin, a tunable valley degree of freedom. This renders these materials promising candidates for valleytronics [1–4], where the valley relaxation time T_1 is an important figure of merit, allowing us to assess the potential for valley-based information storage. In 2D transition metal dichalcogenides with moderate band gaps, the valley degree of freedom is very accessible for optical manipulation and readout. This allowed pump-probe spectroscopy experiments [5,6], in particular time-resolved Kerr rotation experiments [7–11], which revealed relaxation times ranging from nanoseconds to microseconds, depending on the material and excitation conditions. However, such optical techniques are not readily applicable to narrow gap bilayer graphene (BLG), resulting in a lack of knowledge about valley lifetimes in BLG. Recent advances in the confinement of carriers in BLG using quantum dots (QDs), however, are opening up new avenues for the study of valley lifetimes in BLG.

Bernal-stacked BLG comes as a gapless semimetal, in which electrons and holes can be described as massive Dirac fermions [12]. However, when an out-of-plane electric displacement field D is applied, the inversion symmetry of the crystal lattice is broken, as the on-site energy of carbon atoms of the top layer becomes different from that of the atoms of the bottom layer [see Fig. 1(a)] [13]. This leads to the opening of a band gap at the two valleys, K and K' [see Fig. 1(b)], which depends on the strength of the symmetry breaking potential, i.e., on D [14–16], resulting in a tunable band structure that allows for gate-defined charge carrier confinement [17–19]. The broken inversion symmetry also leads to a finite Berry curvature Ω near the K points, where Ω has opposite signs at the K and K' points and has mirror symmetry for electrons and holes [13,20] [see Fig. 1(c)]. The Berry curvature gives rise to a valley-dependent anomalous velocity term leading to the valley-Hall effect in bulk BLG [21,22] and to finite out-of-plane magnetic moments in BLG QDs. These topological orbital magnetic moments, which have opposite signs for K and K', couple to an external out-of-plane magnetic field and are the origin of the valley Zeeman effect in BLG QDs [23,24].

To create gate-defined QDs in BLG, the electronic wave function needs to be confined by a potential $U(\mathbf{r})$ in real space [see Fig. 1(a)] and will be distributed near the K and K' points in k space. A single-electron or single-hole QD can then be described by the Hamiltonian $H_{\mathrm{QD}} = H_{\mathrm{BLG}} + H_Z + H_{\mathrm{SO}} + U(\mathbf{r})$ [25]. Here, H_{BLG} represents the effective 4×4 Hamiltonian of bulk BLG near the K and K' points based on the sublattice and layer degrees of freedom and includes the bulk valley Zeeman effect (see Appendix A), which will be further modified by the confinement $U(\mathbf{r})$. H_Z denotes the spin Zeeman coupling. H_{SO} describes the intrinsic Kane-Mele spin-orbit (SO) coupling, which lifts the zero B field degeneracy of the four single-particle states, leading to the formation of two Kramers pairs with opposite spin and valley quantum numbers ($|K\uparrow\rangle$, $|K'\downarrow\rangle$) and ($|K'\uparrow\rangle$, $|K\downarrow\rangle$), separated by the SO gap Δ_{SO}. In BLG devices Δ_{SO} typically has values in the

---

[*] These authors contributed equally to this work.

[†] Present address: Faculty of Physics, University of Vienna, Boltzmanngasse 5, 1090 Vienna, Austria.

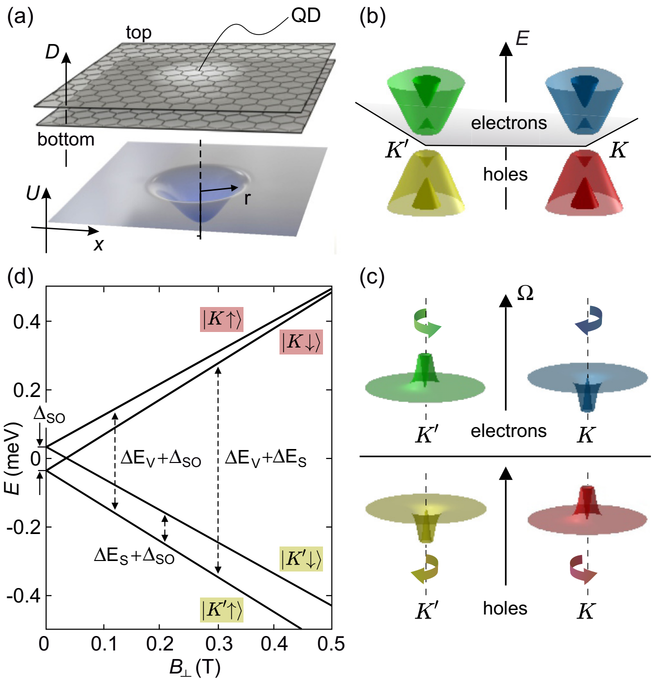

FIG. 1. (a) Lattice structure of BLG highlighting the top and bottom layers and a symmetry breaking displacement field D. The electrostatic confinement potential U allows us to form a QD. (b) Band structure of gapped BLG. Close to the K and the K' valleys a band gap opens. (c) The broken inversion symmetry results in a finite Berry curvature Ω near the K and K' points, which has opposite signs for the two valleys and for electrons and holes. (d) Single-particle spectrum of a BLG QD. At $B_\perp = 0$, Δ_{SO} leads to the formation of two Kramers doublets. A finite $B_\perp$ results in a spin and valley Zeeman effect, leading to additional energy splittings of $\Delta E_{\mathrm{s}} = g_{\mathrm{s}}\mu_{\mathrm{B}}B$ and $\Delta E_{\mathrm{v}} = g_{\mathrm{v}}\mu_{\mathrm{B}}B$. The arrows depict the transition energies between the ground state $|K'\uparrow\rangle$ and the three excited states.

range of 40–80 μeV [18,20,23,26,27]. In Fig. 1(d) we show the single-particle spectrum of a BLG hole QD as a function of the out-of-plane magnetic field $B_\perp$. As $B_\perp$ couples to both the spin and valley magnetic moments, we observe linear energy shifts given by $E(B_\perp) - E(0) = (\pm g_{\mathrm{s}} \pm g_{\mathrm{v}})\mu_{\mathrm{B}}B_\perp/2$ [28]. Here, μ_{B} is the Bohr magneton, $g_{\mathrm{s}} \approx 2$ is the spin g factor, and the valley g factor g_{v} quantifies the strength of the Berry curvature induced valley magnetic moment, which can be tuned by the confinement potential of the QD in a range typically between $g_{\mathrm{v}} \approx 10$ and 70 [24,29,30]. All this makes the valley degree of freedom in BLG QDs highly tunable, in stark contrast to its behavior in Si, Ge, and SiGe QDs, enabling significant valley polarization at relatively low $B_\perp$ fields, which is evident from the separation between the $|K'\rangle$ and excited $|K\rangle$ states shown in Fig. 1(d).

II. RESULTS

The fabricated device consists of a flake of BLG encapsulated by two crystals of hexagonal boron nitride (hBN) placed on a graphite flake acting as a back gate. On top of the van der Waals heterostructure, split gates (SGs) are used to gap out the BLG underneath, resulting in a narrow n-type conductive channel connecting the source (S) and drain (D) leads [see Fig. 2(a)]. To confine single charge carriers, the band edge profile along the channel can be adjusted using two layers of interdigitated finger gates (FGs) [17,19]. One of the FGs is used as a plunger gate (PG) to tune the QD, locally overcompensating for the channel potential set by the back gate. The width of the PG measures about 70 nm, and the separation of the SGs is around 80 nm, setting an upper limit of the QD radius r to around 30–40 nm. The DC potential applied to the plunger gate V_{PG} allows us to control the charge carrier occupation down to the last hole [see Fig. 2(b)]. To study transient transport through the QD, an AC potential, V_{AC}, can be applied to the PG via a bias tee [see Fig. 2(a)]. To maximize the transient currents and to study the relaxation dynamics of the QD states, the FGs adjacent to the PG (yellow and blue) are used to reduce the tunnel coupling between the QD and the left and right reservoirs, Γ_{L} and Γ_{R} [31–34]. The details of the device fabrication and the experimental setup are given in Appendixes B and C.

To study the relaxation dynamics of an excited valley state, we first investigate the single-particle spectrum of the QD. For that purpose, we perform excited state transient current spectroscopy measurements by applying a square pulse with a frequency f (duty cycle 50%) to the PG [see Fig. 2(c)]. Figure 2(d) shows the average number of charge carriers tunneling through the QD per pulse cycle, $\langle n\rangle/\mathrm{pulse} = I/(fe)$, with the elementary charge e, as a function of the pulse amplitude V_{AC} and the DC plunger gate voltage ΔV_{PG} relative to the Coulomb peak position at $V_{\mathrm{AC}} = 0$. At finite V_{AC}, transport via the ground state (GS) may occur when the GS resides within the bias window during either part of the square pulse (τ_{i}, τ_{m}), resulting in a splitting of the GS Coulomb peak ($|K\uparrow\rangle_{\mathrm{i}}$ and $|K\uparrow\rangle_{\mathrm{m}}$) [32,35]. Once V_{AC} becomes large enough that an excited state (ES) enters the bias window, a transient current via the ES contributes to the overall current and shows up as a resonance in Fig. 2(d) (see dashed lines). From the positions of the two prominent ES resonances we can extract their energies. Figure 2(e) depicts the energy difference between the ground state ($|K'\uparrow\rangle$) and the first spin ES (yellow data points, $|K'\downarrow\rangle$) and the valley ESs (red data points, $|K\downarrow\rangle$ and $|K\uparrow\rangle$) determined from measurements in Fig. 2(d) as a function of $B_\perp$. The energy splitting of the spin ES and the GS increases linearly with $B_\perp$ due to the spin Zeeman effect. A fit to the data yields a spin g factor of $g_{\mathrm{s}} = 2.0 \pm 0.2$ and a zero-field splitting of $\Delta_{\mathrm{SO}} = 75$ μeV, in agreement with the slightly proximity-enhanced Kane-Mele SO coupling [20,23,26]. Due to the finite peak width, the energy of the two valley ESs cannot be determined independently. Thus, the data were fit considering the average energy splitting with a slope corresponding to $g_{\mathrm{v}} + g_{\mathrm{s}}/2$. A valley g factor of $g_{\mathrm{v}} = 30.2 \pm 0.2$ was determined, similar to values reported in earlier works [23,24].

Next, to investigate the relaxation dynamics of the observed single-particle valley ES, we apply a three-level pulse scheme to the PG [see Fig. 3(a)] and measure the tunneling current through the QD [33]. During τ_{i}, the QD is initialized in the empty state. Subsequently, during τ_{h}, the GS $|K'\uparrow\rangle$, the spin ES $|K'\downarrow\rangle$, and the two valley ESs, $|K\uparrow\rangle$ and $|K\downarrow\rangle$, are tuned below the electrochemical potentials of the source and drain leads. After the characteristic tunneling time, on the order of $1/(\Gamma_{\mathrm{L}} + \Gamma_{\mathrm{R}})$, either the GS or one of the three ESs will be occupied by a single charge carrier.

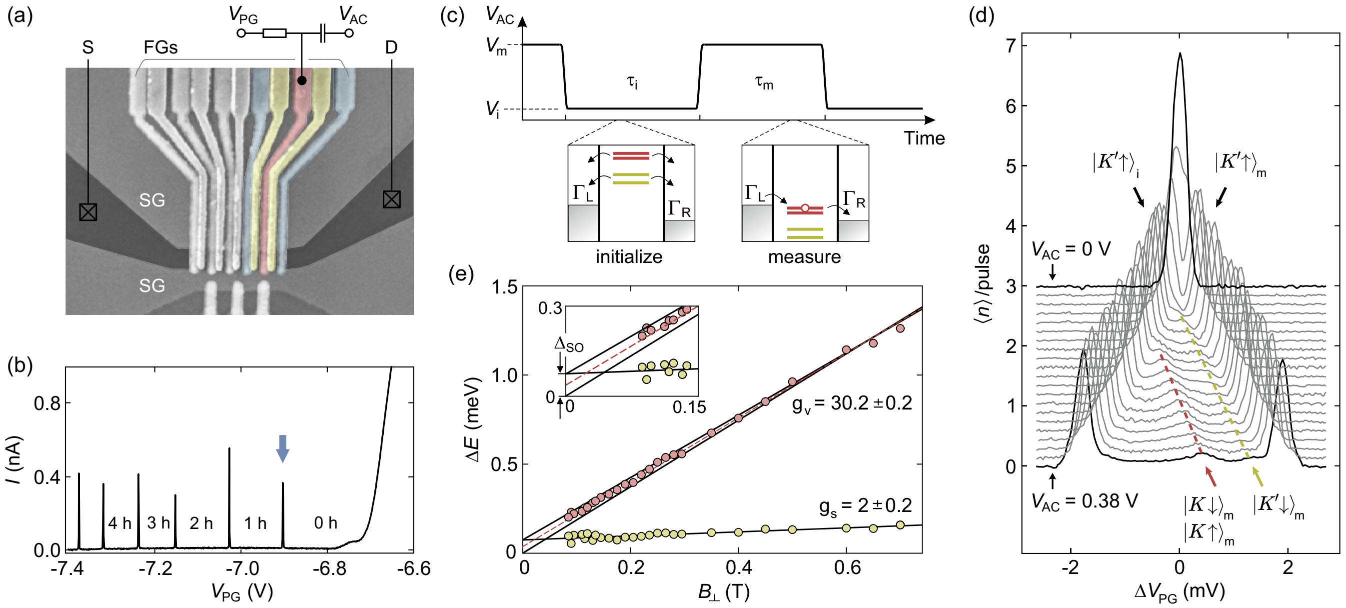

FIG. 2. (a) False-color scanning electron microscopy image of the gate structure of the device. The plunger gate (PG, red) is connected to a bias tee for applying AC and DC signals to the same gate. (b) Current through the device as a function of V_{PG} at a source-drain bias voltage of $V_{SD} = 200\ \mu V$. The n-type channel is pinched off close to $V_{PG} = -6.8$ V. Upon further decreasing V_{PG}, a hole QD is formed, and Coulomb resonances appear when additional holes are added to the QD (see labels). (c) Top: Schematic of the square pulse applied to the PG characterized by the voltages V_i and V_m and the times τ_i and τ_m. Bottom: Schematic of the QD states relative to the electrochemical potentials of the leads. (d) Excited state (ES) spectroscopy using transient current measurements. The average number of charge carriers $\langle n \rangle$ tunneling through the QD per pulse is plotted as a function of ΔV_{PG} for different V_{AC} ($f = 5$ MHz, $B_\perp = 300$ mT). Traces are offset for clarity. $|K'\uparrow\rangle$ denotes the current via the ground state. Orange and yellow dashed lines highlight transient currents via excited states ($|K'\downarrow\rangle$, $|K\uparrow\rangle$, and $|K\downarrow\rangle$). (e) Energy ΔE of the ES relative to the GS as a function of $B_\perp$. Fitting $\Delta_{SO}/2 + (g_v + g_s/2)\mu_B B$ (orange dashed line) yields g_v. The solid lines indicate the energies of the valley ESs deduced from the fits. The inset shows a close-up of the low-$B_\perp$ regime.

A charge carrier in an ES has the chance to relax into an energetically lower-lying state by either spin or valley relaxation with a characteristic relaxation time T_1. Finally, during τ_m, we perform a valley-selective readout, measured by aligning the $|K\rangle$ states in the bias window. Only charge carriers occupying one of the two $|K\rangle$ states, which have not relaxed into a $|K'\rangle$ state, can tunnel out and contribute to the transient current. Figure 3(b) shows the current I through the QD as a function of V_{PG} while applying the pulse sequence depicted in Fig. 3(a). The three peaks labeled $|K'\uparrow\rangle_i$, $|K'\uparrow\rangle_h$, and $|K'\uparrow\rangle_m$ correspond to GS transport during each of the three pulse steps. Furthermore, transient currents via the three ESs, $|K\uparrow\rangle_m$, $|K\downarrow\rangle_m$, and $|K'\downarrow\rangle_m$, can be observed during τ_m. The relaxation time T_1 of the $|K\rangle$ states into an energetically lower-lying state can be probed by extracting the maximum value of the combined $|K\uparrow\rangle_m$ and $|K\downarrow\rangle_m$ peaks, which at a fixed value of $B_\perp$ is at a constant energy difference [see Fig. 1(d)], as a function of the holding time τ_h (for more information on the peak analysis see Appendix D) [31,33,34]. We convert the current I into the number of charge carriers tunneling through the QD per pulse cycle, $\langle n \rangle/\text{pulse} = I(\tau_i + \tau_h + \tau_m)/e$. The number of charge carriers $\langle n \rangle_{|K\rangle_m}$ tunneling via the excited $|K\rangle$ states is directly proportional to the probability of $|K\rangle$ remaining occupied after τ_h, $P_{|K\rangle}(\tau_h)$. The relative occupation probability of $|K\rangle_m$ as a function of τ_h decays exponentially with the characteristic relaxation time T_1, $\langle n \rangle_{|K\rangle_m}(\tau_h)/\langle n \rangle_{|K\rangle_m}(0) = P_{|K\rangle}(\tau_h)/P_{|K\rangle}(0) = e^{-\tau_h/T_1}$ [31,33].

Figure 3(c) depicts $P_{|K\rangle}(\tau_h)/P_{|K\rangle}(0)$ as a function of τ_h for three different out-of-plane magnetic fields. The datasets show an exponential decay of the occupation probability as a function of τ_h. An exponential fit (solid line) yields, for example, $T_1 = 4.0\ \mu s$ at $B_\perp = 0.175$ T. T_1 decreases with increasing $B_\perp$ and reaches a value of 845 ns at $B_\perp = 0.45$ T. A single charge carrier occupying $|K\uparrow\rangle$ or $|K\downarrow\rangle$ may relax into a lower-lying state either by pure valley relaxation ($|K\uparrow\rangle \rightarrow |K'\uparrow\rangle$ and $|K\downarrow\rangle \rightarrow |K'\downarrow\rangle$) or by additionally flipping the spin ($|K\uparrow\rangle \rightarrow |K'\downarrow\rangle$ and $|K\downarrow\rangle \rightarrow |K'\uparrow\rangle$). Relaxation processes requiring a single valley flip are expected to be faster than processes that require both a spin flip and a valley flip. This is supported by recently reported spin relaxation times between hundreds of microseconds and 50 ms for energy splittings $\Delta E_S > 200\ \mu eV$ [33,34]. For the pure spin relaxation between $|K'\downarrow\rangle$ and the GS, no relaxation could be observed over the whole range of investigated τ_h and $B_\perp$ (the amplitude of $|K'\downarrow\rangle_m$ is constant as a function of τ_h; see Appendix D). Hence, we conclude that T_1 extracted from Fig. 3(c) must be limited by the valley relaxation time.

In Fig. 4, we plot the valley relaxation time T_1 extracted from exponential fits, as exemplarily shown in Fig. 3(c) as a function of $B_\perp$ and as a function of the energy splitting ΔE_v. When decreasing $B_\perp$ from 0.7 to about 0.15 T, T_1 increases from below 0.5 to about 7 μs, while at even lower $B_\perp$, the relaxation rate decreases again to $T_1 \sim 2$ μs at 80 mT (gray symbols).

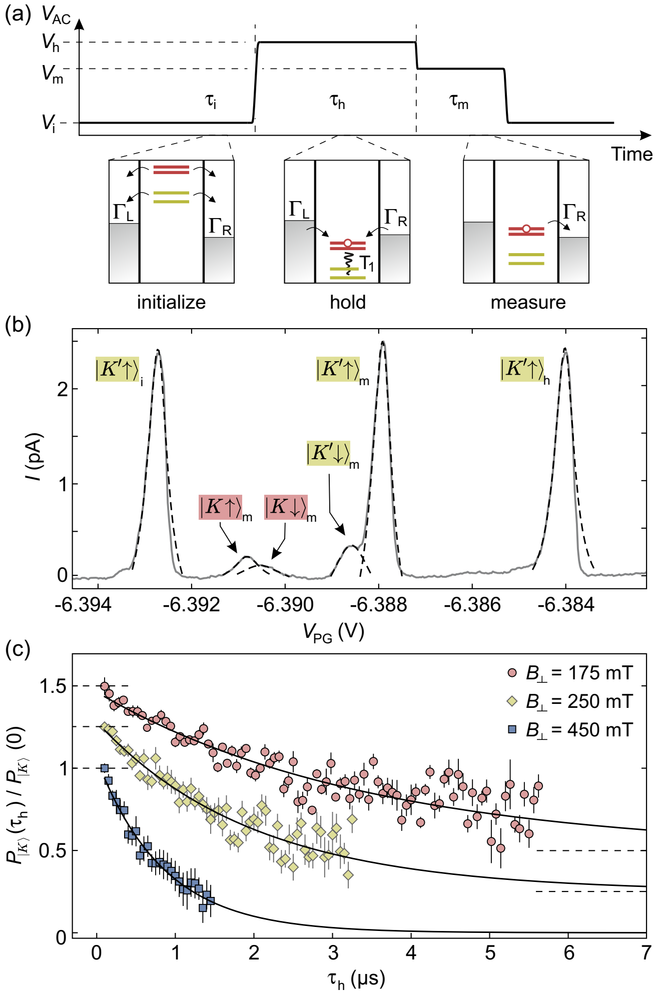

FIG. 3. (a) Top: Schematic of the three-level pulse scheme applied to the PG, which is characterized by the voltages $V_{\rm i}$, $V_{\rm h}$, and $V_{\rm m}$ and the times $\tau_{\rm i}$, $\tau_{\rm h}$, and $\tau_{\rm m}$. Bottom: Schematic of the QD states relative to the electrochemical potentials in the leads (see text for details). (b) Current I as a function of $V_{\rm PG}$ while the pulse sequence in (a) is applied ($B_\perp = 0.22\,{\rm T}$, $V_{\rm SD} = 10\,\mu{\rm V}$). The valley T_1 time is derived from the amplitude of $|K\uparrow\rangle_{\rm m}$. Dashed curves are Lorentzian fits to the peaks. (c) Relative occupation probability of $|K\uparrow\rangle$ after the holding pulse $P_{|K\rangle}(\tau_{\rm h})/P_{|K\rangle}(0)$ as a function of the holding time, $\tau_{\rm h}$. The traces are offset for clarity.

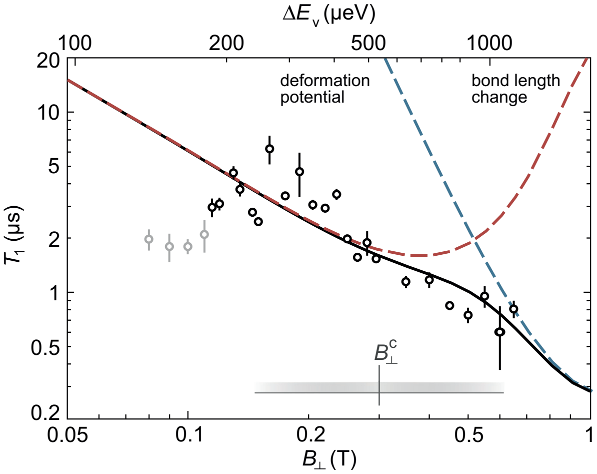

FIG. 4. Valley relaxation time T_1 as a function of $B_\perp$ (bottom axis) and the valley splitting $\Delta E = g_{\rm v}\mu_{\rm B}B_\perp$ (top axis). Error bars indicate the 1σ confidence interval of an exponential fit to the data as in Fig. 3(c). The black curve represents a fit assuming T_1 is limited by electron-phonon coupling arising from the deformation potential and from bond length change. The blue (red) curve shows the contribution of the deformation potential (bond length change) separately.

III. THEORETICAL MODEL

To gain a better understanding of the experimental results, we compare them with theory. We model the system using the Hamiltonian $H = H_{\rm QD} + H_{\rm EPC} + H_{KK'}$, where $H_{\rm QD}$ describes a single electron or hole in the BLG QD and $H_{\rm EPC} = \sum_{\lambda q} H_{\rm EPC}^{\lambda q}$ is the electron-phonon coupling. Furthermore, we allow mixing between the two valleys described by the intervalley coupling term $H_{KK'} = \Delta_{KK'}\tau_x/2$, with the Pauli matrix τ_x acting on the valley degree of freedom. For simplicity, we model electrostatic confinement using a finite circularly symmetric step potential $U(\mathbf{r})$ with potential depth $U_0 \approx 39.6\,{\rm meV}$ and $r = 25\,{\rm nm}$. This yields a valley g factor of $g_{\rm v} = 30$, in good agreement with the experiment [see Fig. 2(e)]. We consider transitions between states with equal spin but opposite valley degrees of freedom mediated by coupling to in-plane acoustic phonons arising either from the deformation potential (coupling strength g_1) or from bond length change (g_2) [36]. Since we operate in the low-energy limit, we consider only acoustic phonons, while out-of-plane acoustic (ZA) phonons are supposed to be quenched in graphene supported on a substrate, especially in encapsulated graphene [25,37]. The Hamiltonian describing coupling to phonons in mode λ with wave vector q has the form $H_{\rm EPC}^{\lambda q} = c_q(g_1 a_1\sigma_0 + g_2 a_2'\sigma_x + g_2 a_2''\sigma_y)(e^{i\mathbf{q}\cdot\mathbf{r}}b_{\lambda q}^\dagger - e^{-i\mathbf{q}\cdot\mathbf{r}}b_{\lambda q})$, with $\sigma_{x,y,z}$ being the Pauli matrices for the sublattice degree of freedom [38,39] and $c_q = \sqrt{q/A\rho v_\lambda}$, with A being the area of the BLG sheet, ρ being the mass density of BLG, and v_λ being the sound velocity; $a_{1,2}$ are phase factors, and $b_{\lambda q}$ and $b_{\lambda q}^\dagger$ are the phonon ladder operators [25]. Using Fermi's golden rule, we calculate the valley relaxation times T_1 between the initial and final eigenstates $|i\rangle$ and $|f\rangle$ of the Hamiltonian $H_{\rm QD} + H_{KK'}$ with opposite valley quantum numbers and eigenenergies ε_i and ε_f,

$$\frac{1}{T_1} = 2\pi A \sum_\lambda \int \frac{d^2q}{(2\pi)^2} |\langle i| H_{\rm EPC}^{\lambda q} |f\rangle|^2 \delta(\varepsilon_f - \varepsilon_i + v_\lambda q).$$

We take into account only the emission of phonons (with energy $v_\lambda q$) because the thermal energy is significantly smaller than the valley splitting. To quantify the electron-phonon coupling strength, we perform the least squares fit to the experimental data using g_1 and g_2 as free fit parameters. Our model is in good qualitative and quantitative agreement with the data taken above $B_\perp = 0.1\,{\rm T}$, where increasing $B_\perp$ results in decreasing T_1, but it cannot explain the decrease in T_1 observed for $B_\perp < 0.1\,{\rm T}$, suggesting that other mechanisms dominate in this regime. We speculate that the discrepancy between our model and the data in the regime $B_\perp < 0.1\,{\rm T}$ may be due to a hot spot [40], thermal broadening induced charge noise [41,42], or $1/f$ charge noise, which is expected to become dominant in the small energy range, as discussed in more detail in Ref. [25]. Consequently, we have restricted the fit to the data for $B_\perp \geqslant 0.1\,\mathrm{T}$, which yields coupling parameters of $g_1 = 50$ eV and $g_2 = 5.4$ eV. It is noteworthy that both parameters are in good agreement with the literature, which includes values in the range of 20–50 eV for g_1 [43–47] and values in the range of 1.5–5 eV for g_2 [36,47], where the wide range of values is partly due to the dependence of the deformation potential on screening and doping [43,44]. The black solid line in Fig. 4 corresponds to the contributions from both the deformation potential coupling and bond length change coupling, while the dashed lines show the individual contributions (see labels). In the calculation, the intervalley coupling, which is mainly responsible for the absolute values of T_1 but does not enter the functional $B_\perp$ dependence, was set to $\Delta_{KK'} = 50\ \mu\mathrm{eV}$. At larger magnetic fields, $B_\perp \gtrsim 0.5$ T, T_1 is predominantly limited by electron-phonon coupling via the deformation potential, whereas at smaller fields it is limited by the coupling due to bond length change. This transition occurs due to the crossover between the dipole and the higher multipole regimes for the bond length change coupling if the phonon wavelength $\lambda \approx 2\pi\hbar v_\lambda/(g_v\mu_B B_\perp)$ is comparable to the QD radius r, where $qr = 2\pi r/\lambda \approx 1$. Hence, the crossover occurs around the critical field $B_\perp^c \approx \hbar v_\lambda/(g_v\mu_B r) \approx 0.3$ T. The assumed QD radius of $r = 25$ nm is in agreement with the lithographic device dimensions as well as with the confinement size, giving rise to a valley g factor of $g_v = 30$, in excellent agreement with experiment. The gray bar in Fig. 4 depicts the range of $B_\perp^c$ assuming the estimate of r deviates by a factor of 2, highlighting that the transition region is well within the experimentally investigated $B_\perp$ range.

IV. DISCUSSION AND RESULTS

The long single-particle valley lifetimes in BLG QDs of up to 7 μs make BLG a promising candidate for valleytronic applications and confirm that the valley degree of freedom is, indeed, interesting for the realization of qubits, where the T_1 time sets an upper limit on the coherence time T_2^*. This potential is furthermore underlined by a recent experiment showing long relaxation times from valley triplet to valley singlet states [48]. Fits to the experimental data confirm that electron-phonon coupling mediated by the bond length change and the deformation potential limit the relaxation time over a wide magnetic field range. As the valley magnetic moment is typically 1 to 2 orders of magnitude larger than the magnetic moment associated with the electron spin, we anticipate that gate operation times of a valley qubit are much faster than those of a spin qubit, potentially compensating for the shorter relaxation times. The magnitude of the valley magnetic moment can be adjusted all electrically [30], which could provide a way to realize control over a single valley without the need for microwave bursts, micromagnets, or electron spin resonance strip lines and could enable well-controlled addressability. Crucial follow-up experiments include the determination of the coherence times (T_2^* and T_2) and insights into their limiting mechanisms such as charge noise, as well as the understanding of the upper bound of the recently reported long relaxation times of Kramers states at small energy splittings [49].

ACKNOWLEDGMENTS

The authors thank A. Hosseinkhani for fruitful discussions and F. Lentz, S. Trellenkamp, M. Otto, and D. Neumaier for help with sample fabrication. This project has received funding from the European Research Council (ERC) under Grant Agreement No. 820254, the Deutsche Forschungsgemeinschaft (DFG, German Research Foundation) under Germany's Excellence Strategy - Cluster of Excellence Matter and Light for Quantum Computing (ML4Q) EXC 2004/1-390534769 through DFG (STA 1146/11-1), and the Helmholtz Nano Facility [50]. K.W. and T.T. acknowledge support from the JSPS KAKENHI (Grants No. 21H05233 and No. 23H02052), CREST (JPMJCR24A5), JST, and the World Premier International Research Center Initiative (WPI), MEXT, Japan. L.W. and G.B. acknowledge support from DFG Project No. 425217212, SFB 1432.

C.S. designed and directed the project. L.B., K.H., and S.M. fabricated the device. L.B., K.H., and C.V. performed the measurements and analyzed the data. K.W. and T.T. synthesized the hBN crystals. L.W. and G.B. performed calculations of the T_1 time. G.B., C.V., and C.S. supervised the project. L.B., K.H., L.W., G.B., C.V., and C.S. wrote the manuscript with contributions from all authors.

The authors declare no competing interests.

DATA AVAILABILITY

The data that support the findings of this article are openly available [51].

APPENDIX A: HAMILTONIAN OF BILAYER GRAPHENE

The Hamiltonian H_{BLG} used to describe the band structure of bulk BLG is given by

$$H_{\mathrm{BLG}}(\mathbf{k}) = \begin{bmatrix} \Delta & \gamma_0 p & \gamma_4 p* & \gamma_1 \\ \gamma_0 p* & \Delta & \gamma_3 p & \gamma_4 p* \\ \gamma_4 p & \gamma_3 p* & -\Delta & \gamma_0 p \\ \gamma_1 & \gamma_4 p & \gamma_0 p* & -\Delta \end{bmatrix}, \tag{A1}$$

with the displacement field being 2Δ and the hopping parameters $\gamma_0 = 2.6\,\mathrm{eV}$, $\gamma_1 = 0.339\,\mathrm{eV}$, $\gamma_3 = 0.28\,\mathrm{eV}$, and $\gamma_4 = -0.14\,\mathrm{eV}$. The momentum $p(\mathbf{k}) = -\sqrt{3}a(\tau k_x - ik_y - ixB_\perp e/2 - \tau y B_\perp e/2)/2$, with valley index $\tau = \pm 1$ and lattice constant $a = 2.46$ Å, includes the valley Zeeman effect [13,52,53].

APPENDIX B: DEVICE FABRICATION

The device is composed of a van der Waals heterostructure, where a BLG flake is encapsulated between two hBN flakes approximately 25 nm thick and placed on a graphite flake which acts as a back gate (BG). Cr/Au split gates on top of the heterostructure define an 80 nm wide channel. Across the channel, two layers of 70 nm wide interdigitated Cr/Au finger gates are fabricated. Two 15 nm thick layers of atomic layer deposited $\mathrm{Al_2O_3}$ act as a gate dielectric. For the details of the fabrication process, we refer to Ref. [54].

APPENDIX C: EXPERIMENTAL SETUP AND PARAMETERS

In order to perform RF gate modulation, the sample is mounted on a home-built printed circuit board. All DC lines are low pass filtered (10 nF capacitors to ground). All FGs are connected to onboard bias tees, allowing for AC and DC control on the same gate [see Fig. 2(a)]. All AC lines are equipped with cryogenic attenuators of −26 dB. V_{AC} refers to the AC voltage applied prior to attenuation. The measurements are performed in a ^{3}He/^{4}He dilution refrigerator at a base temperature of approximately 20 mK and at an electron temperature of around 60 mK. The current through the device is amplified and converted into a voltage with a home-built *I*-*V* converter at a gain of 10^8.

Throughout the experiment, a constant back gate voltage of $V_{\mathrm{BG}} = 5.025$ V and a split gate voltage of $V_{\mathrm{SG}} = -5.435$ V are applied to define an *n*-type channel between the source and the drain. The four gates acting as barrier gates to the QD [see Fig. 2(a), yellow and blue color coding] are biased by -6.05 ± 0.1, -4.95, -5.18, and -6.15 ± 0.1 V, respectively. The voltages are adjusted to compensate for the influence of $B_\perp$ on the tunnel coupling.

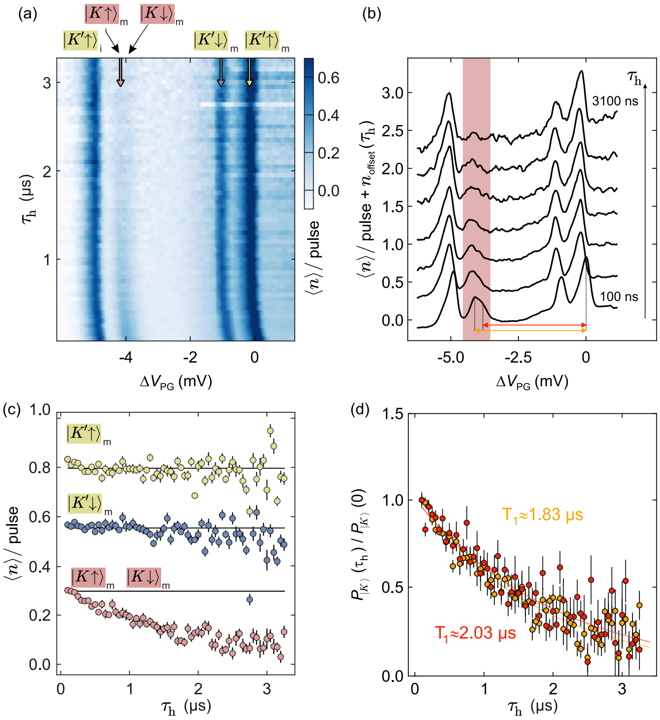

FIG. 5. (a) Average number of charge carriers $\langle n\rangle$ tunneling through the device per pulse cycle (derived from the current *I*) as a function of V_{PG} and τ_{h} while the pulse sequence depicted in Fig. 3(a) is applied. The color-coded arrows mark the positions of the peaks $|K'\uparrow\rangle_{\mathrm{m}}$ (yellow), $|K'\downarrow\rangle_{\mathrm{m}}$ (blue), and $|K\downarrow\rangle_{\mathrm{m}}$ and $|K\uparrow\rangle_{\mathrm{m}}$ (red). An out-of-plane magnetic field of $B_\perp = 0.25$ T was applied. (b) Exemplary line traces of the measurement in (a), where $\langle n\rangle$/pulse is shown as a function of V_{PG} for different values of τ_{h} (black arrow on the right side). The traces are offset by an arbitrary n_{offset} for better visibility. (c) Maximum values of the labeled peaks in (a) as a function of the pulse duration τ_{h}. The maximum value of the peak that we attribute to $|K\downarrow\rangle_{\mathrm{m}}$ and $|K\uparrow\rangle_{\mathrm{m}}$ was extracted in a voltage window at a fixed energy difference from the peak $|K'\uparrow\rangle_{\mathrm{m}}$ [red shaded area in (b)]. (d) Normalized occupation probability extracted at fixed energy splittings corresponding to the two $|K\rangle$ states [red and orange arrows in (b)].

APPENDIX D: PEAK ANALYSIS AND EXTRACTING RELAXATION TIMES

Figure 5(a) shows an exemplary measurement of the average number of charge carriers $\langle n\rangle$ tunneling through the QD per pulse cycle as a function of the duration of the holding pulse τ_{h} and the plunger gate voltage V_{PG}. The colored labels mark the probed states. The measurement was recorded at an out-of-plane magnetic field of $B_\perp = 0.25$ T [the measurement corresponds to the results depicted in Fig. 3(c)]. Exemplarily, line cuts of the measurement in Fig. 5(a) are shown in Fig. 5(b). The peak heights of $|K'\uparrow\rangle_{\mathrm{m}}$ and $|K'\downarrow\rangle_{\mathrm{m}}$ are displayed in Fig. 5(c) as a function of the pulse duration τ_{h}. The maximum value of the peak attributed to $|K\uparrow\rangle_{\mathrm{m}}$ and $|K\downarrow\rangle_{\mathrm{m}}$ [red data points in Fig. 5(c)] is extracted in a small voltage window at a fixed distance from the position of the peak $|K'\uparrow\rangle_{\mathrm{m}}$ [visualized by the red shaded area in Fig. 5(b)].

It is important to note that the observed exponential decay does not depend on details of the peak analysis. The line cuts in Fig. 5(b) reveal that the finite peak linewidth compared to the small energy spacing between the $|K\rangle$ states makes it difficult to identify peaks $|K\downarrow\rangle_{\mathrm{m}}$ and $|K\uparrow\rangle_{\mathrm{m}}$ independently. Therefore, we extracted the maximum value of the combined peak contributions [red shaded area in Fig. 5(b)]. To highlight that the obtained result is robust, we determine the values at fixed energy splittings from the ground state peak $|K'\uparrow\rangle_{\mathrm{m}}$, $\Delta E_{\mathrm{V}} + \Delta E_{\mathrm{S}}$ [red arrow in Fig. 5(b)] and $\Delta E_{\mathrm{V}} + \Delta_{\mathrm{SO}}$ [orange arrow in Fig. 5(b)], which correspond to the expected positions of peaks $|K\downarrow\rangle_{\mathrm{m}}$ and $|K\uparrow\rangle_{\mathrm{m}}$, respectively. The corresponding normalized occupation probabilities as a function of τ_{h} are shown in Fig. 5(d). The results yield similar decay constants ($T_1 \approx 2.03$ μs and $T_1 \approx 1.83$ μs) which are within the margin of the error of the results shown in Fig. 4. Apart from the exponential decay of the maximum value at $|K\downarrow\rangle_{\mathrm{m}}$ and $|K\uparrow\rangle_{\mathrm{m}}$ [see also Fig. 3(c)], the peaks of the ground state ($|K'\uparrow\rangle_{\mathrm{m}}$) and the first excited state ($|K'\downarrow\rangle_{\mathrm{m}}$) show a constant maximum value over the measured range of τ_{h}. Since spin relaxation, from $|K'\downarrow\rangle$ to $|K'\uparrow\rangle$, would show up in a decrease of the peak height of $|K'\downarrow\rangle_{\mathrm{m}}$ [blue data points in Fig. 5(c)], we conclude that spin relaxation appears on a timescale $\tau_{\mathrm{h}} \gg 3$ μs. This observation aligns with previous findings [33,34].

---

[1] A. Rycerz, J. Tworzydło, and C. W. J. Beenakker, Valley filter and valley valve in graphene, Nat. Phys. **3**, 172 (2007).

[2] J. R. Schaibley, H. Yu, G. Clark, P. Rivera, J. S. Ross, K. L. Seyler, W. Yao, and X. Xu, Valleytronics in 2D materials, Nat. Rev. Mater. **1**, 16055 (2016).

[3] F. Bussolotti, H. Kawai, Z. E. Ooi, V. Chellappan, D. Thian, A. L. C. Pang, and K. E. J. Goh, Roadmap on finding chiral valleys: Screening 2D materials for valleytronics, Nano Futures **2**, 032001 (2018).

[4] M. S. Mrudul, Á. Jiménez-Galán, M. Ivanov, and G. Dixit, Light-induced valleytronics in pristine graphene, Optica **8**, 422 (2021).

[5] J. Kim, C. Jin, B. Chen, H. Cai, T. Zhao, P. Lee, S. Kahn, K. Watanabe, T. Taniguchi, S. Tongay, M. F. Crommie, and F. Wang, Observation of ultralong valley lifetime in WSe_2/MoS_2 heterostructures, Sci. Adv. **3**, e1700518 (2017).

[6] C. Mai, A. Barrette, Y. Yu, Y. G. Semenov, K. W. Kim, L. Cao, and K. Gundogdu, Many-body effects in valleytronics: Direct measurement of valley lifetimes in single-layer MoS_2, Nano Lett. **14**, 202 (2014).

[7] W.-T. Hsu, Y.-L. Chen, C.-H. Chen, P.-S. Liu, T.-H. Hou, L.-J. Li, and W.-H. Chang, Optically initialized robust valley-polarized holes in monolayer WSe_2, Nat. Commun. **6**, 8963 (2015).

[8] P. Dey, L. Yang, C. Robert, G. Wang, B. Urbaszek, X. Marie, and S. A. Crooker, Gate-controlled spin-valley locking of resident carriers in WSe_2 monolayers, Phys. Rev. Lett. **119**, 137401 (2017).

[9] L. Yang, N. A. Sinitsyn, W. Chen, J. Yuan, J. Zhang, J. Lou, and S. A. Crooker, Long-lived nanosecond spin relaxation and spin coherence of electrons in monolayer MoS_2 and WS_2, Nat. Phys. **11**, 830 (2015).

[10] T. Yan, S. Yang, D. Li, and X. Cui, Long valley relaxation time of free carriers in monolayer WSe_2, Phys. Rev. B **95**, 241406(R) (2017).

[11] S. Zhao, X. Li, B. Dong, H. Wang, H. Wang, Y. Zhang, Z. Han, and H. Zhang, Valley manipulation in monolayer transition metal dichalcogenides and their hybrid systems: Status and challenges, Rep. Prog. Phys. **84**, 026401 (2021).

[12] K. S. Novoselov, E. McCann, S. V. Morozov, V. I. Fal'ko, M. I. Katsnelson, U. Zeitler, D. Jiang, F. Schedin, and A. K. Geim, Unconventional quantum Hall effect and Berry's phase of 2π in bilayer graphene, Nat. Phys. **2**, 177 (2006).

[13] E. McCann and M. Koshino, The electronic properties of bilayer graphene, Rep. Prog. Phys. **76**, 056503 (2013).

[14] J. B. Oostinga, H. B. Heersche, X. Liu, A. F. Morpurgo, and L. M. K. Vandersypen, Gate-induced insulating state in bilayer graphene devices, Nat. Mater. **7**, 151 (2008).

[15] Y. Zhang, T.-T. Tang, C. Girit, Z. Hao, M. C. Martin, A. Zettl, M. F. Crommie, Y. R. Shen, and F. Wang, Direct observation of a widely tunable bandgap in bilayer graphene, Nature (London) **459**, 820 (2009).

[16] E. Icking, L. Banszerus, F. Wörtche, F. Volmer, P. Schmidt, C. Steiner, S. Engels, J. Hesselmann, M. Goldsche, K. Watanabe, T. Taniguchi, C. Volk, B. Beschoten, and C. Stampfer, Transport spectroscopy of ultraclean tunable band gaps in bilayer graphene, Adv. Electron. Mater. **8**, 2200510 (2022).

[17] M. Eich, F. Herman, R. Pisoni, H. Overweg, A. Kurzmann, Y. Lee, P. Rickhaus, K. Watanabe, T. Taniguchi, M. Sigrist, T. Ihn, and K. Ensslin, Spin and valley states in gate-defined bilayer graphene quantum dots, Phys. Rev. X **8**, 031023 (2018).

[18] L. Banszerus, B. Frohn, T. Fabian, S. Somanchi, A. Epping, M. Müller, D. Neumaier, K. Watanabe, T. Taniguchi, F. Libisch, B. Beschoten, F. Hassler, and C. Stampfer, Observation of the spin-orbit gap in bilayer graphene by one-dimensional ballistic transport, Phys. Rev. Lett. **124**, 177701 (2020).

[19] L. Banszerus, B. Frohn, A. Epping, D. Neumaier, K. Watanabe, T. Taniguchi, and C. Stampfer, Gate-defined electron–hole double dots in bilayer graphene, Nano Lett. **18**, 4785 (2018).

[20] L. Banszerus, S. Möller, K. Hecker, E. Icking, K. Watanabe, T. Taniguchi, F. Hassler, C. Volk, and C. Stampfer, Particle–hole symmetry protects spin-valley blockade in graphene quantum dots, Nature (London) **618**, 51 (2023).

[21] Y. Shimazaki, M. Yamamoto, I. V. Borzenets, K. Watanabe, T. Taniguchi, and S. Tarucha, Generation and detection of pure valley current by electrically induced Berry curvature in bilayer graphene, Nat. Phys. **11**, 1032 (2015).

[22] M. Sui, G. Chen, L. Ma, W.-Y. Shan, D. Tian, K. Watanabe, T. Taniguchi, X. Jin, W. Yao, D. Xiao, and Y. Zhang, Gate-tunable topological valley transport in bilayer graphene, Nat. Phys. **11**, 1027 (2015).

[23] L. Banszerus, S. Möller, C. Steiner, E. Icking, S. Trellenkamp, F. Lentz, K. Watanabe, T. Taniguchi, C. Volk, and C. Stampfer, Spin-valley coupling in single-electron bilayer graphene quantum dots, Nat. Commun. **12**, 5250 (2021).

[24] C. Tong, R. Garreis, A. Knothe, M. Eich, A. Sacchi, K. Watanabe, T. Taniguchi, V. Fal'ko, T. Ihn, K. Ensslin, and A. Kurzmann, Tunable valley splitting and bipolar operation in graphene quantum dots, Nano Lett. **21**, 1068 (2021).

[25] L. Wang and G. Burkard, Valley relaxation in a single-electron bilayer graphene quantum dot, Phys. Rev. B **110**, 035409 (2024).

[26] A. Kurzmann, Y. Kleeorin, C. Tong, R. Garreis, A. Knothe, M. Eich, C. Mittag, C. Gold, F. K. de Vries, K. Watanabe, T. Taniguchi, V. Fal'ko, Y. Meir, T. Ihn, and K. Ensslin, Kondo effect and spin–orbit coupling in graphene quantum dots, Nat. Commun. **12**, 6004 (2021).

[27] C. Tong, A. Kurzmann, R. Garreis, W. W. Huang, S. Jele, M. Eich, L. Ginzburg, C. Mittag, K. Watanabe, T. Taniguchi, K. Ensslin, and T. Ihn, Pauli blockade of tunable two-electron spin and valley states in graphene quantum dots, Phys. Rev. Lett. **128**, 067702 (2022).

[28] A. Knothe and V. Fal'ko, Influence of minivalleys and Berry curvature on electrostatically induced quantum wires in gapped bilayer graphene, Phys. Rev. B **98**, 155435 (2018).

[29] S. Möller, L. Banszerus, A. Knothe, C. Steiner, E. Icking, S. Trellenkamp, F. Lentz, K. Watanabe, T. Taniguchi, L. I. Glazman, V. I. Fal'ko, C. Volk, and C. Stampfer, Probing two-electron multiplets in bilayer graphene quantum dots, Phys. Rev. Lett. **127**, 256802 (2021).

[30] S. Möller, L. Banszerus, A. Knothe, L. Valerius, K. Hecker, E. Icking, K. Watanabe, T. Taniguchi, C. Volk, and C. Stampfer, Impact of competing energy scales on the shell-filling sequence in elliptic bilayer graphene quantum dots, Phys. Rev. B **108**, 125128 (2023).

[31] R. Hanson, B. Witkamp, L. M. K. Vandersypen, L. H. W. van Beveren, J. M. Elzerman, and L. P. Kouwenhoven, Zeeman energy and spin relaxation in a one-electron quantum dot, Phys. Rev. Lett. **91**, 196802 (2003).

[32] L. Banszerus, K. Hecker, E. Icking, S. Trellenkamp, F. Lentz, D. Neumaier, K. Watanabe, T. Taniguchi, C. Volk, and C. Stampfer, Pulsed-gate spectroscopy of single-electron spin states in bilayer graphene quantum dots, Phys. Rev. B **103**, L081404 (2021).

[33] L. Banszerus, K. Hecker, S. Möller, E. Icking, K. Watanabe, T. Taniguchi, C. Volk, and C. Stampfer, Spin relaxation in a single-electron graphene quantum dot, Nat. Commun. **13**, 3637 (2022).

[34] L. M. Gächter, R. Garreis, J. D. Gerber, M. J. Ruckriegel, C. Tong, B. Kratochwil, F. K. de Vries, A. Kurzmann, K. Watanabe, T. Taniguchi, T. Ihn, K. Ensslin, and W. W. Huang, Single-shot spin readout in graphene quantum dots, PRX Quantum **3**, 020343 (2022).

[35] T. Fujisawa, Y. Tokura, and Y. Hirayama, Transient current spectroscopy of a quantum dot in the Coulomb blockade regime, Phys. Rev. B **63**, 081304(R) (2001).

[36] T. Sohier, M. Calandra, C.-H. Park, N. Bonini, N. Marzari, and F. Mauri, Phonon-limited resistivity of graphene by first-principles calculations: Electron-phonon interactions, strain-induced gauge field, and Boltzmann equation, Phys. Rev. B **90**, 125414 (2014).

[37] P. R. Struck and G. Burkard, Effective time-reversal symmetry breaking in the spin relaxation in a graphene quantum dot, Phys. Rev. B **82**, 125401 (2010).

[38] T. Ando, Theory of electronic states and transport in carbon nanotubes, J. Phys. Soc. Jpn. **74**, 777 (2005).

[39] E. Mariani and F. von Oppen, Flexural phonons in free-standing graphene, Phys. Rev. Lett. **100**, 076801 (2008).

[40] C. H. Yang, A. Rossi, R. Ruskov, N. S. Lai, F. A. Mohiyaddin, S. Lee, C. Tahan, G. Klimeck, A. Morello, and A. S. Dzurak, Spin-valley lifetimes in a silicon quantum dot with tunable valley splitting, Nat. Commun. **4**, 2069 (2013).

[41] P. Huang and X. Hu, Electron spin relaxation due to charge noise, Phys. Rev. B **89**, 195302 (2014).

[42] A. Hosseinkhani and G. Burkard, Relaxation of single-electron spin qubits in silicon in the presence of interface steps, Phys. Rev. B **104**, 085309 (2021).

[43] C.-H. Park, N. Bonini, T. Sohier, G. Samsonidze, B. Kozinsky, M. Calandra, F. Mauri, and N. Marzari, Electron–phonon interactions and the intrinsic electrical resistivity of graphene, Nano Lett. **14**, 1113 (2014).

[44] E. Mariani and F. von Oppen, Temperature-dependent resistivity of suspended graphene, Phys. Rev. B **82**, 195403 (2010).

[45] J.-H. Chen, C. Jang, S. Xiao, M. Ishigami, and M. S. Fuhrer, Intrinsic and extrinsic performance limits of graphene devices on $\mathrm{SiO_2}$, Nat. Nanotechnol. **3**, 206 (2008).

[46] E. H. Hwang and S. D. Sarma, Acoustic phonon scattering limited carrier mobility in two-dimensional extrinsic graphene, Phys. Rev. B **77**, 115449 (2008).

[47] H. Suzuura and T. Ando, Phonons and electron-phonon scattering in carbon nanotubes, Phys. Rev. B **65**, 235412 (2002).

[48] R. Garreis, C. Tong, J. Terle, M. J. Ruckriegel, J. D. Gerber, L. M. Gächter, K. Watanabe, T. Taniguchi, T. Ihn, K. Ensslin, and W. W. Huang, Long-lived valley states in bilayer graphene quantum dots, Nat. Phys. **20**, 428 (2024).

[49] A. O. Denisov, V. Reckova, S. Cances, M. J. Ruckriegel, M. Masseroni, C. Adam, C. Tong, J. D. Gerber, W. W. Huang, K. Watanabe, T. Taniguchi, T. Ihn, K. Ensslin, and H. Duprez, Spin–valley protected Kramers pair in bilayer graphene, Nat. Nanotechnol. **20**, 494 (2025).

[50] W. Albrecht, J. Moers, and B. Hermanns, HNF - Helmholtz Nano Facility, J. Large-Scale Res. Facil. **3**, 112 (2017).

[51] L. Banszerus, K. Hecker, L. Wang, S. Möller, K. Watanabe, T. Taniguchi, G. Burkard, C. Volk, and C. Stampfer, Zenodo (2025), doi:10.5281/zenodo.15643611.

[52] S. Konschuh, M. Gmitra, D. Kochan, and J. Fabian, Theory of spin-orbit coupling in bilayer graphene, Phys. Rev. B **85**, 115423 (2012).

[53] L. Wang and M. W. Wu, Electron spin relaxation in bilayer graphene, Phys. Rev. B **87**, 205416 (2013).

[54] L. Banszerus, A. Rothstein, T. Fabian, S. Möller, E. Icking, S. Trellenkamp, F. Lentz, D. Neumaier, K. Watanabe, T. Taniguchi, F. Libisch, C. Volk, and C. Stampfer, Electron–hole crossover in gate-controlled bilayer graphene quantum dots, Nano Lett. **20**, 7709 (2020).